

Article

Quasi-Classical Trajectory Dynamics Study of the Reaction $\text{OH} + \text{H}_2\text{S} \rightarrow \text{H}_2\text{O} + \text{SH}$ and Its Isotopic Variants: Comparison with Experiment

Zhao Tu ^{1,2}, Jiaqi Li ^{2,3}, Yan Wang ^{1,*} and Hongwei Song ^{2,*}¹ School of Chemical and Environmental Engineering, Hubei Minzu University, Enshi 445000, China² State Key Laboratory of Magnetic Resonance and Atomic and Molecular Physics, Innovation Academy for Precision Measurement Science and Technology, Chinese Academy of Sciences, Wuhan 430071, China³ College of Physical Science and Technology, Huazhong Normal University, Wuhan 430079, China

* Correspondence: hbwangy@sohu.com (Y.W.); hwsong@wipm.ac.cn (H.S.)

Abstract: The hydrogen abstraction reaction $\text{OH} + \text{H}_2\text{S} \rightarrow \text{H}_2\text{O} + \text{SH}$ plays an important role in acid rain formation, air pollution and climate change. In this work, the product energy disposals of the reaction and its isotopic variants $\text{OD} + \text{H}_2\text{S}$ and $\text{OD} + \text{D}_2\text{S}$ are calculated on a new ab-initio-based ground electronic state potential energy surface (PES) using the quasi-classical trajectory method. The PES is developed by fitting a total of 72,113 points calculated at the level of UCCSD(T)-F12a/aug-cc-pVTZ and using the fundamental invariant-neural network method, resulting in a total RMSE of 4.14 meV. The product H_2O formed in the $\text{OH} + \text{H}_2\text{S}$ reaction at 298 K is found to be largely populated in the first overtone states of its symmetric and asymmetric stretching modes, while the vibrational distributions of the products HOD and D_2O in the isotopically substituted reactions are visibly different. The computed product vibrational state distributions agree reasonably well with experimental results and are rationalized by the sudden vector projection model.

Keywords: hydrogen abstraction; energy disposal; $\text{OH} + \text{H}_2\text{S}$ reaction; isotopic substitution; potential energy surface



Citation: Tu, Z.; Li, J.; Wang, Y.; Song, H. Quasi-Classical Trajectory Dynamics Study of the Reaction $\text{OH} + \text{H}_2\text{S} \rightarrow \text{H}_2\text{O} + \text{SH}$ and Its Isotopic Variants: Comparison with Experiment. *Symmetry* **2023**, *15*, 256. <https://doi.org/10.3390/sym15020256>

Academic Editor: Anthony Harriman

Received: 28 December 2022

Revised: 12 January 2023

Accepted: 14 January 2023

Published: 17 January 2023



Copyright: © 2023 by the authors. Licensee MDPI, Basel, Switzerland. This article is an open access article distributed under the terms and conditions of the Creative Commons Attribution (CC BY) license (<https://creativecommons.org/licenses/by/4.0/>).

1. Introduction

Hydrogen sulfide (H_2S), as a well-known toxic gas and environmental pollutant, causes acid rain formation, some human and animal diseases and climate change [1,2]. The loss of H_2S in the atmosphere is mainly by reacting with hydroxyl radical ($\cdot\text{OH}$), i.e., a typical representative of hydrogen abstraction reactions [2–9]. Accurate determination of the rate constant is important for constructing atmospheric chemical models. The $\text{OH} + \text{H}_2\text{S} \rightarrow \text{H}_2\text{O} + \text{SH}$ reaction is also thought to be the first stage in the oxidation of H_2S , which possibly evolves into sulfuric acid or sulfate aerosol [10]. Therefore, much attention has been paid to studying the kinetics and dynamics of the $\text{OH} + \text{H}_2\text{S} \rightarrow \text{H}_2\text{O} + \text{SH}$ reaction both experimentally [11–22] and theoretically [23–29].

The rate constant of the reaction was measured to be $(3.1\text{--}5.7) \times 10^{-12} \text{ cm}^3 \text{ molecule}^{-1} \text{ s}^{-1}$ at 298 K and found to have a non-Arrhenius temperature dependence at relatively low and high temperatures [11,12,14–16,30,31]. Butkovskaya and Setser [19–21] studied the vibrational excitation of the product molecules from the reactions of OH and OD radicals with H_2S at 298 K in a fast-flow reactor by modeling infrared emission spectra at 0.5 Torr of Ar, in which the dynamics associated with the energy disposal were analyzed.

Theoretically, Benjamin and Truhlar attributed the unusual temperature dependence to a dynamical bottleneck by direct dynamics at the level of M06-2X/MG3S and then investigated the kinetic isotope effects of the $\text{OH} + \text{D}_2\text{S}$ and $\text{OD} + \text{D}_2\text{S}$ reactions [25]. The interaction between OH radical and H_2S has been investigated by different first-principle methods [25,27,32,33]. A complex $\text{H}_2\text{S} \cdots \text{OH}$ was predicted to be formed by the two center

and triple electron S-O bond (2c-3e) [32,33]. In 2017, Tang et al. studied the minimum energy path using the ‘gold standard’ CCSD(T) method with Dunning’s aug-cc-pV(X+d)Z (X = D, T, Q, 5) [27]. The barrier height was calculated to be 0.11 kcal mol⁻¹ at the level of CCSD(T)/aug-cc-pV(5+d)Z with the geometries optimized at the level of aug-cc-pV(Q+d)Z. In 2018, some of the authors [28] constructed a global, full-dimensional potential energy surface (PES) for the OH + H₂S → H₂O + SH reaction and studied the kinetics and dynamics of the reaction using the quasi-classical trajectory (QCT) method. Quantum dynamics calculations on the PES showed that fundamental excitations of either the symmetric or the asymmetric stretching modes of H₂S have similar and remarkable efficacy on promoting the reactivity, while exciting the bending mode slightly enhances the reaction at low collision energies, and the enhancement effect increases with the collision energy [29]. Although the PES is accurate and smooth, it is not suitable for simulating experimental conditions at 298 K due to the relatively short asymptotic region. The furthest distance between reactants (or products) from the sampled data points in the work was only 8 Å.

In this work, we construct a new full-dimensional and globally accurate ground electronic state PES. The PES can accurately describe the interaction between the reactants OH and H₂S (or products) as far as 25 Å, which is sufficiently enough for simulating Butkovskaya and Setser’s experiment by QCT theory. The PES is fitted by the fundamental invariant-neural network (FI-NN) method [34] based on 72,113 ab initio points at the level of UCCSD(T)-F12a/aug-cc-pVTZ. The vibrational state distributions of products (H₂O/HOD/D₂O) in the OH + H₂S reaction and its isotopic variants are calculated by the normal mode analysis (NMA) method [35–38] on the new PES and compared with available experimental results.

2. Potential Energy Surface

The PES is constructed as follows. The stationary points along the minimum energy path are first optimized at the level of UCCSD(T)-F12a/aug-cc-pVTZ [39,40] by the software Molpro 2012 [41]. Secondly, in order to obtain enough initial points, a batch of grid points are generated along the minimum energy path, with the condition that the grid points meet the energy range of −1.5–2.0 eV and the reactant (product) separation is less than 25 Å. Then, atom-centered density matrix propagation (ADMP) molecule dynamics are performed from each grid point at the level of M06-2X/6-31 + G(d) by the software Gaussian 09 [42]. The initial data points from the ADMP trajectories must be selected by the Euclidean distance, which is defined in terms of the bond lengths, $\Delta D = \sqrt{\sum_{i=1}^n (\vec{r}_i - \vec{r}'_i)^2}$ (\vec{r}_i and \vec{r}'_i represent the nuclear distances of the reserved configuration in the data set and the new configuration, n represents the number of bonds). The permutationally equivalent points are also included in such a screening. Different from our previous work, the value of Euclidean distance is well designed in this work. The sampled configuration space is divided into three parts: the first part ($0 < \vec{R}_{OH} \leq 3$), where $\Delta D > 0.25$ Å; the second part ($3 < \vec{R}_{OH} \leq 7$), where a linear function defined as $\Delta D > (\vec{R}_{OH} - 3.0) \times 0.04 + 0.25$ is employed; and the third part ($7 < \vec{R}_{OH} \leq 25$), where $\Delta D > 0.41$ Å, \vec{R}_{OH} is the longest bond in OH bond. Clearly, the new scheme to choose the value of Euclidean distance adjusts the density of the sample data points according to the varying of potential energy, which can save the computational cost of ab initio calculations. Thirdly, the FI-NN method is applied to fit the initial data set to generate a raw PES. Due to the lack of data points in some regions, artificial wells exist in the raw PES. Therefore, quasi-classical trajectories are then launched at a different temperature to get more trajectory points. To fill out artificial wells in the raw PES, a batch of PESs are fitted and are used to assess the error for each point that is defined as $error = \sqrt{\frac{1}{N} \sum_{i=1}^N (E_i - \frac{1}{N} \sum_{i=1}^N E_i)^2}$. N is the number of fitted PESs and here $N = 10$, and E_i is the predicted potential energy by the i th PES. Thus, the sampled data points from quasi-classical trajectories are screened by both the error and the Euclidean

distance. The procedure is repeated several times. Finally, a total of 72,113 points are selected with an energy interval of 3.5 eV.

In the FI-NN fitting, the Morse-like variables $P_{ij} = e^{(-r_{ij}/\alpha)}$ are used to construct the polynomials with α as an adjustable constant, and r_{ij} is the internuclear distance between i th and j th atoms [43,44]. In this work, α is taken as 2.0 Å. Twenty fundamental invariants with a maximum degree of 3 for the A_3BC system exist. The structure of the neural network is 20 (input)-50 (hidden 1)-80 (hidden 2)-1 (output), giving a total of 5 211 parameters. The Levenberg–Marquardt algorithm [45] is used to update weights and biases. The root mean square error (RMSE), defined as $RMSE = \sqrt{\frac{1}{N_{data}} \sum_{i=1}^{N_{data}} (E_{fit} - E_{ab\ initio})^2}$, is used to evaluate the quality of each PES. The data points are divided into two groups, with 95% of the points as the training set and 5% as the validating set. The PESs with the RMSE of two data sets having similar small values are chosen to avoid overfitting. The so-called ensemble approach is used to diminish random errors. The final PES is selected to be the average of the three best PESs with training/validating/maximum RMSEs of 4.68/8.12/219.44, 4.66/9.42/193.21 and 4.75/9.41/220.61 meV. The overall RMSE of the PES is 4.14 meV.

3. Quasi-Classical Trajectory Method

QCT calculations, implemented in the software VENUS 96 [46], are carried out on the new PES. The integral cross-section of the reaction at a specific collision energy E_c is computed by

$$\sigma_r(E_c) = \pi b_{max}^2 \frac{N_r}{N_{tot}}$$

where N_r and N_{tot} are the numbers of reactive and total trajectories, respectively. The maximum impact parameter b_{max} is tested by small batches of trajectories with trial values at each specified initial state. The relative statistical error is given by $\Delta = \sqrt{(N_{tot} - N_r)/N_{tot}N_r}$.

For diatomic product molecules, the vibrational quantum numbers are determined by the Einstein–Brillouin–Keller semi-classical quantization of the action integral. However, for product molecules involving more than two atoms, their vibrational quantum numbers become difficult to determine. At present, there are three methods: the fast Fourier transform [47,48], the adiabatic switching method [49] and the NMA method [50]. The first two methods have some disadvantages in determining vibrational state distributions of polyatomic molecules. For example, the fast Fourier transform integrals are well performed only if the trajectories are quasiperiodic, and the adiabatic switching method is sensitive to the choice of coordinate system and zero-order Hamiltonian. In this work, the NMA method [50,51] is employed to calculate classical action numbers. Traditionally, the geometry, including the Cartesian coordinates \vec{r}_i and momenta \vec{p}_i ($i = 1, \dots, N$) in the center of mass (COM) frame, is extracted from the last step of a trajectory. Due to the harmonic approximation, the deviation from the equilibrium geometry sometimes results in unphysical potential energies, giving invalid classical action numbers. To overcome this problem, the method proposed by our group is implemented in this work, in which the coordinates and velocities are taken from a specific step of each trajectory within the last vibrational period of the product molecule [52–54]. The step is determined by asking the corresponding geometry to have the minimum potential energy in the vibrational period. This scheme guarantees the chosen geometry to resemble the equilibrium geometry. Two binning methods, namely histogram binning (HB) and Gaussian binning (GB) [38,55], are employed to confer a “quantum spirit” on the non-integer classical harmonic action number.

In the QCT calculations, the initial conditions in the dynamics calculations are chosen to be similar to the experiment [19–21]. The initial distance of two reactants (OH and H₂S or OD and H₂S or OD and D₂S) is 24.5 Å. The trajectory is stopped when the separation of the two reactants or products is larger than 25.0 Å. The time step of propagation is set as 0.035 fs. The convergence of total energy is better than 10^{−3} kcal mol^{−1}. The collision energy and the initial ro-vibrational state of H₂S (or D₂S) are sampled from a Boltzmann

distribution at 298 K. The initial states of OH (or OD) are sampled by the traditional semi-classical approach. For each of the three reactions, about 150,000 are launched and the relative statistical errors are all below 5%.

4. Results and Discussion

4.1. Properties of the Potential Energy Surface

Table 1 compares the parameters of the new PES with the previous one [28]. Firstly, due to the employment of the new scheme to choose the value of Euclidean distance, the number of sampled data points is decreased from 82,680 to 72,113. Secondly, the sampled data points in this work cover a larger region, in which the separation of reactants (or products) is up to 25 Å, in sharp contrast to 8 Å for the previous PES. Thirdly, the parameter in Morse-like variables, α , is taken as 2.0. A relatively large value of α should be used when the long-range interaction is strong. Finally, the overall RMSE of the new PES is 4.14 meV, 0.58 meV lower than that of the previous PES.

Table 1. Comparison between previous and new potential energy surfaces.

	Previous [28]	This Work
The size of data set	82,680	72,113
The structure of NN	20-50-80-1	20-50-80-1
Length channel (Å)	8.0	25.0
Morse-like α (Å)	1.2	2.0
Total RMSE	4.72	4.14

The minimum energy path of the $\text{OH} + \text{H}_2\text{S} \rightarrow \text{H}_2\text{O} + \text{SH}$ reaction is illustrated in Figure 1. The ab initio energies are calculated at the level of UCCSD(T)-F12a/aug-cc-pVTZ [40,41]. All energies are given in kcal mol^{-1} and with respect to the reactant asymptote. Clearly, four minima exist in the entrance and exit valleys, in which RC-A and PC-A are formed by hydrogen bond, while RC-B and PC-B are hemibonded complexes with two center and triple electron S-O bond (2c-3e). The interaction of hydrogen bond between H_2S (H_2O) and OH (SH) is slightly stronger than the corresponding hemibond, consistent with Tang et al.'s results [27].

To assess the quality of the fitted PES, the optimized geometries by ab initio calculations, the geometries on the fitted PES and available experimental values are listed in Table 2. On one hand, the geometries of the stationary points at the level of UCCSD(T)-F12a/aug-cc-pVTZ are in accord with the geometries at the level of CCSD(T)/aug-cc-pV(Q+d)Z, where the biggest difference of bond length is 0.255 Å and the biggest difference of angle is 12.7°. On the other hand, the predicted geometries by the PES are also consistent with ab initio results. The deviations from the UCCSD(T)-F12a/aug-cc-pVTZ results are less than 0.171 Å for the bond length and 12.0° for the angle. Table 3 shows the energies and frequencies of the stationary points. To solve the problem of non-convergence, the basis function extrapolation and energy shift are adopted in the calculation of single-point energy, which causes a small difference from Ping et al.'s results [28]. The energy difference between the predicted PES and the corresponding ab initio one of UCCSD(T)-F12a/aug-cc-pVTZ is less than 0.1866 kcal mol^{-1} , and the energy difference between UCCSD(T)-F12a/aug-cc-pVTZ and CCSD(T)/aug-cc-pV(Q+d)Z is less than 0.2425 kcal mol^{-1} [27]. The barrier height on the PES is to be $-0.1381 \text{ kcal mol}^{-1}$, which agrees well with the UCCSD(T)-F12a/aug-cc-pVTZ value of $-0.1201 \text{ kcal mol}^{-1}$, while it is slightly lower than the CCSD(T)/aug-cc-pV(Q+d)Z value of 0.0600 kcal mol^{-1} . The frequency difference is less than 53 cm^{-1} compared with the UCCSD(T)-F12a/aug-cc-pVTZ results and the imaginary frequency of the transition state is the same.

Figure 2 shows the 2D contours of the PES as a function of the breaking HS and the forming OH with the other coordinates fixed at the geometry of the transition state. The energy gap of the fitted PES is from -1.5 eV to 2.0 eV . Clearly, the fitted PES is globally smooth. The insert zooms in the contours near the transition state. The pre- and post-

reaction wells are nicely reproduced by the PES. The fitting errors of the sampled points are plotted in Figure 3. The errors for most of the sampled points are distributed in the range of -20 to 20 meV, with several scattered points as large as 200 meV. Overall, the new PES is globally accurate and satisfies the requirement of dynamics calculations.

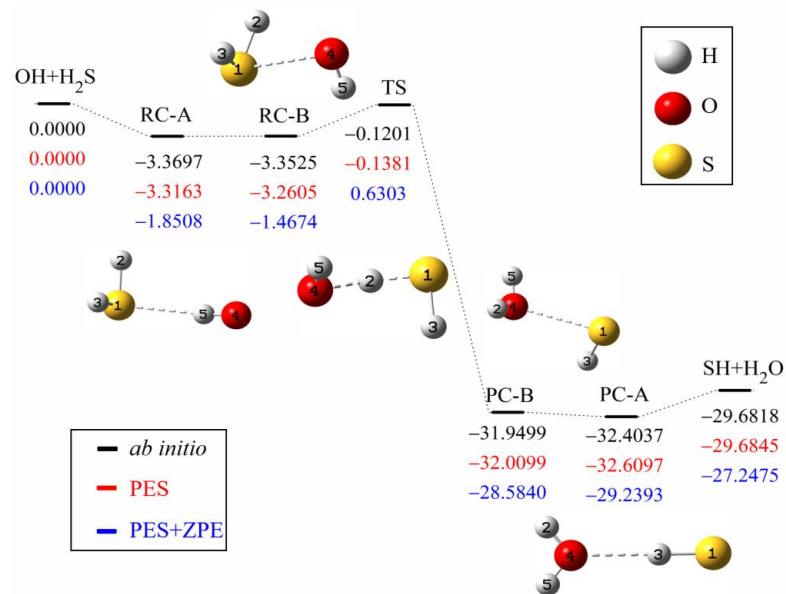


Figure 1. Schematic diagram of the reaction path for the $\text{OH} + \text{H}_2\text{S} \rightarrow \text{H}_2\text{O} + \text{SH}$ reaction. The *ab initio* energies of stationary points at the level of UCCSD(T)-F12a/aug-cc-pVTZ (black) are shown below the corresponding geometries, together with the values of the fitted PES (red) and the zero-point corrected energies (blue). All energies are given in kcal mol^{-1} and relative to the reactant asymptote.

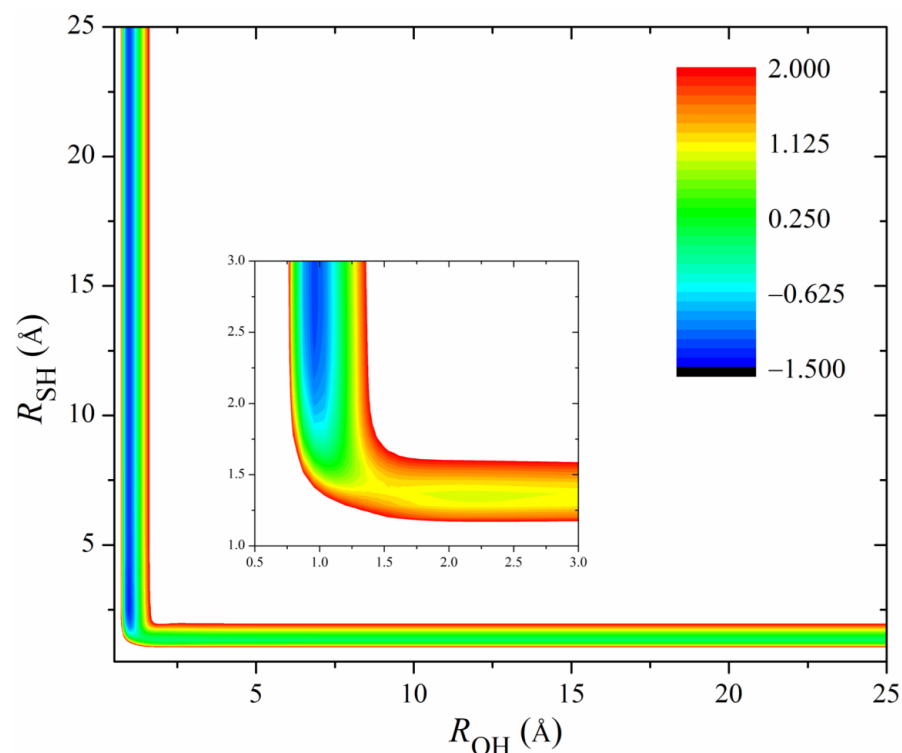


Figure 2. 2D Contours of the PES as a function of the breaking OH and the forming SH with the other coordinates fixed at the geometry of the transition state. The energy gap is from -1.5 to 2.0 eV. The insert zooms in the contours near the transition state with an energy gap from -1.5 to 0.5 eV.

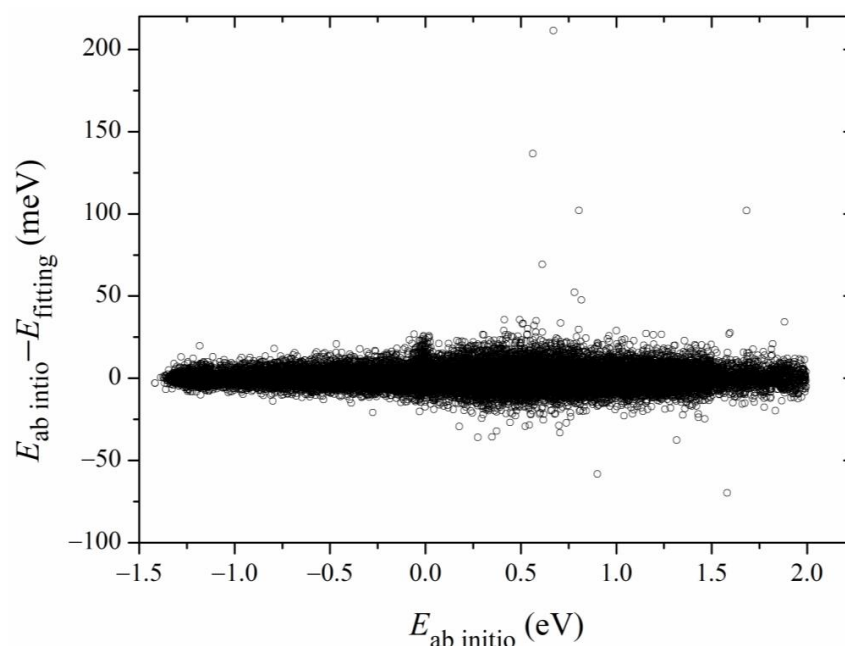


Figure 3. Distributions of fitting errors of the sampled data points.

Table 2. Bond length (in angstrom) and angle (in degree) of stationary points of the reaction $\text{OH} + \text{H}_2\text{S} \rightarrow \text{H}_2\text{O} + \text{SH}$. The atom labels are given in Figure 1.

Species	Method	R_{12}	R_{13}	R_{24}	R_{45}	A_{213}	A_{124}	A_{245}	D_{3124}	D_{1245}
OH	ab initio ^a				0.970					
	ab initio ^b				0.970					
	PES ^c				0.971					
	Expt ^d				0.970					
H ₂ S	ab initio ^a	1.339				92.4				
	ab initio ^b	1.338				92.4				
	PES ^c	1.339				92.6				
	Expt ^d	1.336				92.1				
RC-A	ab initio ^a	1.340	1.340	3.824	0.975	92.5	65.3	23.1	94.2	6.6
	ab initio ^b	1.340	1.340	3.819	0.975	92.5	65.5	23.2	94.2	6.8
	PES ^c	1.340	1.340	3.850	0.976	92.4	64.2	23.1	95.8	−3.6
RC-B	ab initio ^a	1.339	1.339	2.628	0.969	92.5	76.6	105.8	72.7	51.2
	ab initio ^b	1.338	1.338	2.631	0.969	92.6	76.1	106.0	73.2	51.2
	PES ^c	1.338	1.338	2.632	0.969	92.6	74.8	107.4	74.6	51.4
TS	ab initio ^a	1.401	1.340	1.488	0.970	92.1	136.5	102.4	70.8	39.4
	ab initio ^b	1.402	1.339	1.483	0.970	92.2	137.5	102.4	70.8	38.6
	PES ^c	1.398	1.341	1.501	0.971	92.4	134.9	103.3	72.9	43.7
PC-A	ab initio ^a	4.187	1.347	0.959	0.959	10.7	42.1	105.0	0.0	180.0
	ab initio ^b	4.185	1.346	0.959	0.959	10.5	42.0	104.9	0.0	180.0
	PES ^c	4.176	1.347	0.959	0.959	10.6	42.1	105.1	0.0	180.0
PC-B	ab initio ^a	3.163	1.341	0.960	0.959	72.1	73.7	104.7	−61.5	−113.3
	ab initio ^b	3.418	1.340	0.960	0.960	72.8	61.0	104.6	−49.3	−107.6
	PES ^c	3.334	1.341	0.960	0.960	76.8	61.7	104.7	−49.7	−105.9
SH	ab initio ^a	1.343								
	ab initio ^b	1.342								
	PES ^c	1.343								
	Expt ^d	1.341								
H ₂ O	ab initio ^a				0.959			104.4		
	ab initio ^b				0.958			104.4		
	PES ^c				0.959			104.4		
	Expt ^d				0.958			104.5		

^a UCCSD(T)-F12a/aug-cc-pVTZ by Molpro2012, this work; ^b CCSD(T)/aug-cc-pV(Q+d)Z by CFOUR, see Ref. [27]; ^c FI-NN PES, this work; ^d See <http://cccbdb.nist.gov> (accessed on 1 December 2022).

Table 3. Harmonic frequencies (cm^{-1}) and energies (kcal mol^{-1}) of stationary points for the reaction $\text{OH} + \text{H}_2\text{S} \rightarrow \text{H}_2\text{O} + \text{SH}$.

Species	Method	E	1	2	3	4	5	6	7	8	9
OH + H ₂ S	ab initio ^a	0.0000	3738	2736	2720	1212					
	ab initio ^b	0.0000	3739	2738	2722	1212					
	PES ^c	0.0000	3745	2741	2720	1215					
	Expt ^d		3738	2626	2615	1183					
RC-A	ab initio ^a	−3.3697	3653	2732	2715	1210	456	340	165	128	117
	ab initio ^b	−3.3100	3654	2734	2719	1210	440	330	139	136	111
	PES ^c	−3.3163	3641	2726	2711	1210	403	367	148	134	112
RC-B	ab initio ^a	−3.3525	3756	2738	2723	1207	480	259	256	96	72
	ab initio ^b	−3.1100	-	-	-	-	-	-	-	-	-
	PES ^c	−3.2605	3753	2747	2735	1202	503	282	256	126	78
TS	ab initio ^a	−0.1201	3743	2723	1811	1112	719	329	261	186	−858
	ab initio ^b	0.0600	3744	2725	1786	1112	721	326	258	181	−871
	PES ^c	−0.1381	3753	2717	1830	1138	725	331	268	200	−858
PC-A	ab initio ^a	−32.4037	3942	3833	2670	1645	350	192	110	56	−58
	ab initio ^b	−32.4700	3939	3830	2675	1648	347	195	109	74	30
	PES ^c	−32.5903	3952	3843	2679	1656	301	195	108	50	−53
PC-B	ab initio ^a	−31.9499	3929	3818	2712	1644	234	164	132	99	64
	ab initio ^b	−31.7100	-	-	-	-	-	-	-	-	-
	PES ^c	−32.0099	3952	3824	2712	1650	240	166	156	77	63
SH + H ₂ O	ab initio ^a	−29.6818	3942	3832	2696	1646					
	ab initio ^b	−29.5100	3941	3831	2700	1650					
	PES ^c	−29.6845	3943	3830	2694	1647					
	Expt ^d		3756	3657	2696	1595					

^a UCCSD(T)-F12a/aug-cc-pVTZ by Molpro2012, this work; ^b CCSD(T)/aug-cc-pV(Q+d)Z by CFOUR, see Ref. [27]; ^c FI-NN PES, this work; ^d See <http://cccbdb.nist.gov> (accessed on 1 December 2022).

4.2. Product Energy Disposal

Figure 4 shows the calculated product vibrational state distributions. The reactant ro-vibrational states are sampled at 298 K. The three quantum numbers in the parentheses, (ν_1, ν_2, ν_3), denote excitations in the symmetric stretching, bending and asymmetric stretching modes of the products H₂O and D₂O. As to the product HOD, ν_1 refers to excitation in the O-D stretching mode and ν_3 in the O-H stretching mode. Two binning methods (HB and GB) are applied in the calculations. Since the two methods give similar distributions, the following discussions are based on the GB results. For the product molecule H₂O in the OH + H₂S reaction, as shown in Figure 4a, it is mainly populated in the states (200), (002), (012), (210) and (021). The significant excitation of the stretching modes of H₂O results from the visible change of the OH bond among the minimum energy path. The bond length of OH from the transition state to the product H₂O is shortened from 1.501 Å to 0.959 Å. Compared with the stretching modes, the bending mode of H₂O is less excited and mainly populated in the ground and fundamental states.

To study the effect of isotopic substitution on the dynamics, the vibrational state distributions of the products HOD in the reaction OD + H₂S and D₂O in the reaction OD + D₂S are presented in Figure 4b,c, respectively. In sharp contrast to H₂O, the product HOD is dominantly formed in the state (002), i.e., the first overtone of the OH stretching mode, followed by visible excitation in the state (012). The OD bond in the product HOD is nearly unexcited. According to the analysis of the reaction coordinate at the transition state, the stretching motion of the O-H bond is to a great extent along the reaction coordinate. Therefore, the initial available energy favors to flow into the O-H stretching mode of HOD. However, due to the large frequency difference between the OH and OD stretching modes, the intramolecular vibrational redistribution (IVR) is infeasible in the reaction process. In other words, the OD bond is more like a spectator bond in the OD + H₂S reaction. When both reactants OH and H₂S are isotopically substituted, as shown in Figure 4c, the product D₂O is mainly populated in the state (300), followed by (102), (400) and (200). Interestingly,

it appears that the IVR in D₂O is not as strong as in H₂O. The reaction OD + D₂S prefers to produce D₂O in the vibrational excited states of the symmetric stretching mode and the excitation energy in the symmetric stretching mode cannot efficiently flow into the asymmetric stretching mode. In addition, compared with the products H₂O and HOD, D₂O is formed in higher excited states due to its higher density of states. Actually, the products H₂O, HOD and D₂O are all largely populated in the vibrational states whose energies are around 35 kcal mol⁻¹, close to the total available energy.

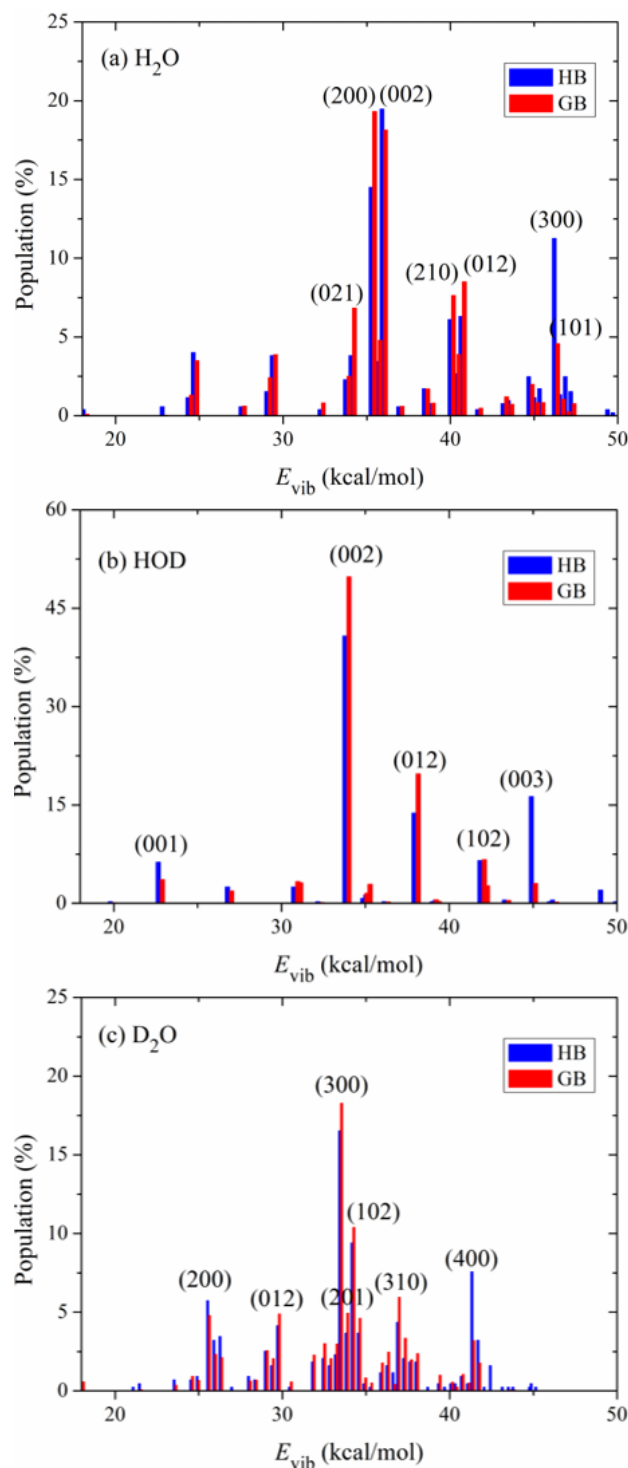


Figure 4. Vibrational state distributions of the products (a) H₂O, (b) HOD and (c) D₂O in the reactions OH + H₂S, OD + H₂S and OD + D₂S, respectively, with the reactants sampled at 298 K.

The vibrational state distributions of the products SH in the reactions OH + H₂S and OD + H₂S and SD in the reaction OD + D₂S are illustrated in Figure 5a–c. Obviously, these products are almost exclusively formed in their ground vibrational states, indicating the nature of a spectator in the reaction OH + H₂S and its isotopic variants.

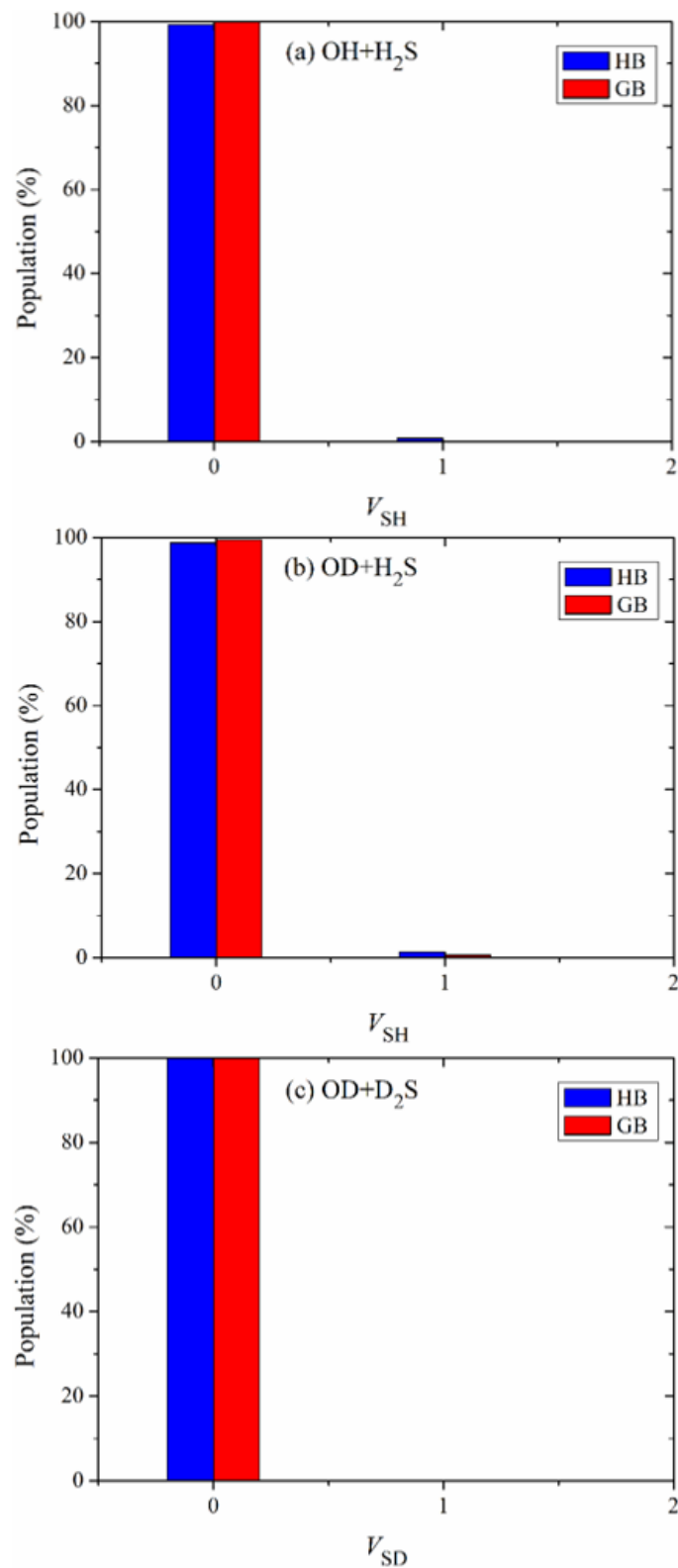


Figure 5. Vibrational state distributions of the products (a) SH, (b) SH and (c) SD in the reactions OH + H₂S, OD + H₂S and OD + D₂S, respectively, with the reactants sampled at 298 K.

Table 4 compares the calculated vibrational state distribution of the product H₂O in the OH + H₂S reaction with the experimental result from Seter's group [19,21]. In the experiment, the symmetric (v_1) and asymmetric (v_3) stretching modes are difficult to distinguish. Thus, $v_{1,3}$ in the table represents the sum of v_1 and v_3 . Theoretical calculations show that the product is largely populated in the states $v_{1,3} = 2$ for $v_2 = 0$ and in the states $v_{1,3} = 1$ for $v_2 = 2$. They are consistent with experimental observations, although visible quantitative difference exists. The theoretical proportion of the states $v_{1,3} = 2$ for $v_2 = 0$ is higher than the corresponding experimental values, while the theoretical proportion of the states $v_{1,3} = 1$ for $v_2 = 2$ is slightly lower. For $v_2 = 1$, the experimental distributions are somewhat scattered, and one experiment gave the highest proportion for the states $v_{1,3} = 2$ [19], consistent with theoretical results; the other experiment reported the highest proportion for the states $v_{1,3} = 1$ [21]. The reactions in the experiment were carried out under the pressure of 0.5 Torr. However, this condition is not considered in theoretical calculations. Therefore, the quantitative difference between experimental and theoretical results is possibly caused by the pressure.

Table 4. Vibrational state distribution of the product H₂O for the reaction OH + H₂S → H₂O + SH.

H ₂ O	v_2								
	0			1			2		
$v_{1,3}$ ^a	Expt1 ^b	Expt2 ^c	Theo	Expt1 ^b	Expt2 ^c	Theo	Expt1 ^b	Expt2 ^c	Theo
0	2.6	2.70	0.000	4.5	2.55	0.087	3.6	2.29	0.009
1	10.3	17.96	4.801	17.7	14.66	6.285	14.3	13.10	9.328
2	24.4	22.77	42.233	20.6	6.54	20.033	0.8	4.90	2.281
3	4.5	1.72	6.632			0.024			

^a $v_{1,3} = v_1 + v_3$; ^b Ref. [19]; ^c Ref. [21].

The vibrational state distribution of the product HOD in the OD + H₂S reaction is listed in Table 5. The quantum numbers v_1 , v_2 and v_3 represent excitations in the OD stretching, bending and OH stretching modes. Since the frequency of OD stretching mode (2831 cm⁻¹) is very close to the double frequency of the bending mode (2888 cm⁻¹), it is hard for the experiment to distinguish them as well. Hence, $v_{1,2}$ in the table is defined as the maximum value of v_1 and v_2 . For $v_{1,2} = 0$, theoretical calculations predict that the product HOD is largely distributed in the state $v_3 = 2$, in accord with the experimental results. On the other hand, both experiment and theory show that the product HOD has larger distributions in $v_3 = 2$ and 1 for $v_{1,2} = 1$ and 2, respectively. In addition, visible difference between experimental and theoretical values also exists.

Table 5. Vibrational state distribution of the product HOD for the reaction OD + H₂S → HOD + SH.

HOD	$v_{1,2}$ ^a								
	0			1			2		
v_3	Expt1 ^b	Expt2 ^c	Theo	Expt1 ^b	Expt2 ^c	Theo	Expt1 ^b	Expt2 ^c	Theo
0	6.3	3.73	0.000	1.1	3.05	0.087	6.3	5.09	0.009
1	9.1	11.75	3.589	4.2	5.08	6.285	10.7	8.72	9.328
2	24.2	27.59	49.767	9.3	8.12	20.033	9.2	5.40	2.281
3	3.0	1.33	3.042			0.024			

^a $v_{1,2}$ is equal to the maximum value of v_1 and v_2 ; ^b Ref. [19]; ^c Ref. [21].

Table 6 lists the vibrational state distribution of the product D₂O in the OD + D₂S reaction. Unfortunately, there are no experimental results for comparison. Like Table 4, $v_{1,3}$ in the table represents the sum of v_1 and v_3 . The product D₂O is largely populated in states $v_{1,3} = 3$ for $v_2 = 0$ and 1. For $v_2 = 2$, D₂O is largely distributed in the states $v_{1,3} = 2$.

Table 6. Vibrational state distribution of the product D₂O for the reaction OD + D₂S → D₂O + SD.

D ₂ O	v ₂		
	0	1	2
v _{1,3} ^a	Theo	Theo	Theo
0	0.0	0.0	0.0
1	0.578	0.071	1.565
2	9.226	9.489	8.022
3	52.079	13.620	1.708

^a v_{1,3} = v₁ + v₃.

The product energy disposals of the three reactions are shown in Figure 6. f_v , f_r and f_t denote the fractions of available energy released as the product vibrational energy, the rotational energy and the translation energy, respectively. The product zero-point energy is subtracted from the corresponding vibrational energy. It can be seen that 68.04% of available energy is released as the vibrational energy of H₂O in the OH + H₂S reaction, followed by the rotational energy of H₂O and the relative translational energy. The small proportion of vibrational and rotational energy of SH indicates that it is hard for the energy to flow into the product SH, no matter the vibrational mode and the rotational mode. When the reactants are isotopically substituted, the product energy disposal is nearly unchanged. Most of available energy flows into the vibrational and rotational modes of HOD in the OD + H₂S reaction or D₂O in the OD + D₂S reaction. It appears that, compared with the former two reactions, a little more energy (12.92%) is transferred as the translational energy in the OD + D₂S reaction. The fraction of $f_v(\text{H}_2\text{O})$ ($f_v(\text{HOD})$) is estimated to be 56% in the experiment [20,21], lower than the calculated value of 69.96% (69.94%). As mentioned, the difference is possibly caused by the pressure of 0.5 Torr in experiment, which is not considered in the simulation.

Although this reaction is likely to be barrierless, the submerged barrier could exert some control on the reactivity, especially for the reactive trajectories by the direct mechanism. The sudden vector projection (SVP) model [56–59] has been widely used to predict reactant mode selectivity and product energy disposal in many gas phase and gas surface reactions by calculating the coupling between the interested reactant or product normal mode vector (\vec{Q}_i) and the reaction coordinate vector (\vec{Q}_{RC}) at the transition state: $P_i = \vec{Q}_i \cdot \vec{Q}_{RC} \in [0, 1]$. The calculated SVP values of different product modes for the three reactions are listed in Table 7. For the OH + H₂S reaction, the symmetric and asymmetric stretching modes of H₂O have the largest projection on the reaction coordinate, followed by the product translational mode and the bending mode of H₂O. The vibrational mode of the product SH has a negligible coupling with the reaction coordinate. This is consistent with QCT calculations, in which the formed H₂O is largely populated in the excited states of the two stretching modes of H₂O, while its bending mode is less excited. Most of available energy flows into the vibrational modes of H₂O, followed by the translational mode, and a very small percentage of the energy is released as the vibrational and rotational energy of SH. For the OD + H₂S reaction, the stretching mode of OH in HOD has the largest projection value, followed by the translational mode and the bending mode of HOD. The stretching mode of OD in HOD has a weak coupling with the reaction coordinate and the vibrational mode of SH has a negligible value. According to QCT calculations, the HOD is dominantly formed in the first overtone state of the OH moiety, well predicted by the SVP model. The product energy disposal of HOD can be explained by the SVP model as well. Furthermore, the SVP values of the product D₂O are close to those of H₂O, indicating similar energy disposal of D₂O to that of H₂O. This is also confirmed by QCT calculations.

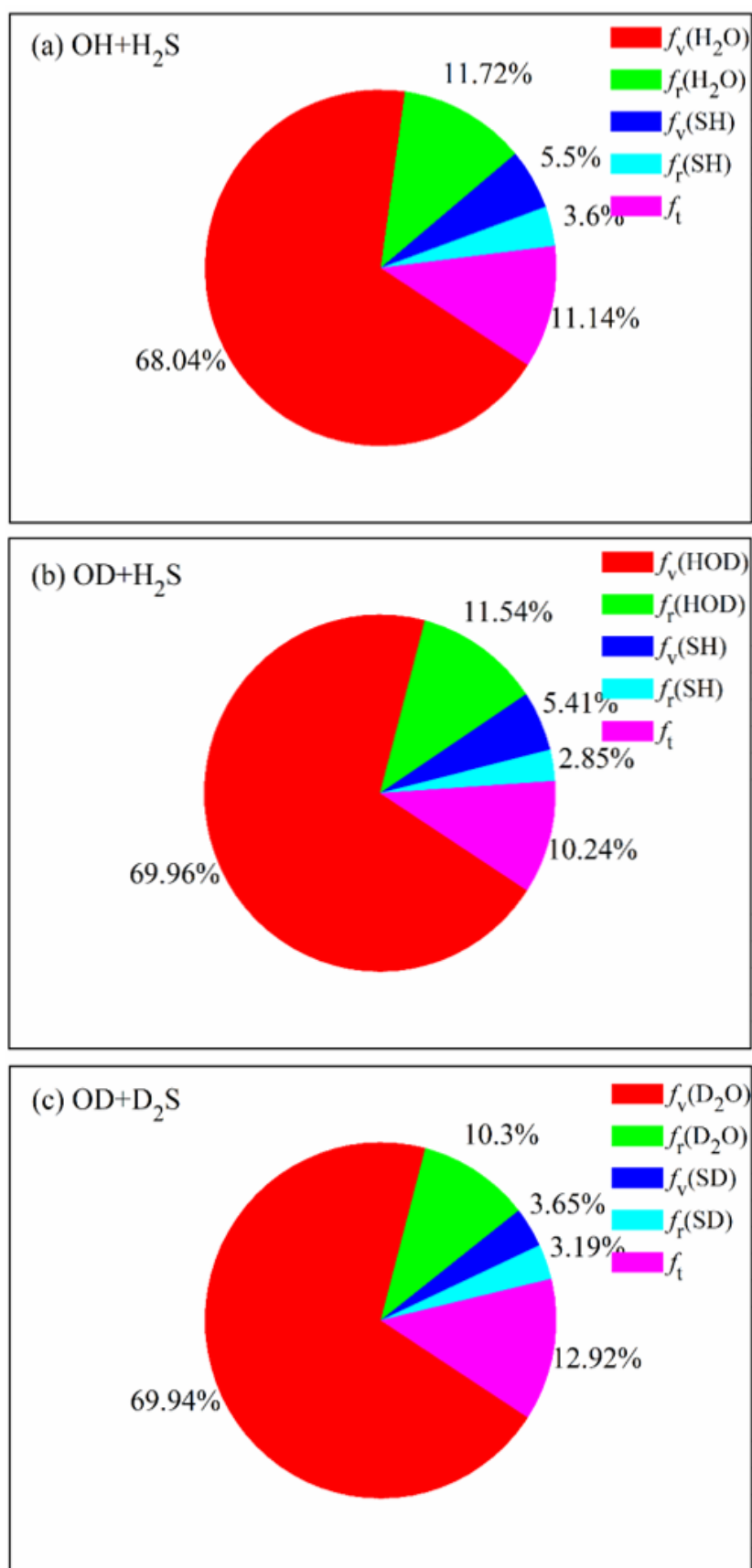


Figure 6. Product energy disposals of the reactions OH + H₂S, OD + H₂S and OD + D₂S with the reactants sampled at 298 K.

Table 7. Sudden vector projection (SVP) values of different product vibrational and translational modes. The numbers ν_1 , ν_2 and ν_3 denote the symmetric, bending and the asymmetric stretching modes of the product H₂O (or D₂O).

SVP					
Species	OH + H ₂ S → H ₂ O + SH	Species	OD + H ₂ S → HOD + SH	Species	OD + D ₂ S → D ₂ O + SD
ν_1	0.672	ν_{OD}	0.068	ν_1	0.680
ν_2	0.106	ν_{bend}	0.135	ν_2	0.102
ν_3	0.657	ν_{OH}	0.936	ν_3	0.660
ν_{SH}	0.002	ν_{SH}	0.002	ν_{SD}	0.003
trans	0.205	trans	0.201	trans	0.212

5. Conclusions

In this work, a full-dimensional, globally accurate PES of the OH + H₂S → SH + H₂O reaction is constructed using the FI-NN method by fitting a total of 72,113 ab initio points calculated at the level of UCCSD(T)-F12a/aug-cc-pVTZ. The fitted PES has a RMSE of 4.14 meV. The geometries and frequencies of the stationary points on the PES agree well with ab initio calculations.

The vibrational state distributions and product energy disposals of the OH + H₂S reaction and its isotopic variants OD + H₂S and OD + D₂S are calculated on the new PES using the QCT method and compared with recent experimental results. Theoretical calculations show that the product H₂O in the OH + H₂S reaction is largely distributed in the first overtone states of its symmetric and asymmetric stretching modes. By contrast, the product HOD is dominantly formed in the first overtone state of the OH stretching mode and the OD moiety is almost unexcited. Compared with the products H₂O and HOD, the product D₂O in the OD + D₂S reaction is formed in higher excited states due to its higher density of states. For all of the three reactions, the products SH and DH are actually unexcited. Most of these conclusions are in reasonable agreement with experimental observations. The quantitative difference between experimental and theoretical distributions is possibly caused by the pressure in the experiment. In addition, most of available energy is released as the vibrational energy of H₂O (or HOD in OD + H₂S or D₂O in OD + D₂S), followed the translational energy. Only a very small proportion of the energy flows into the vibrational and rotational energy of SH (or SD). The dynamical behavior can be well rationalized by the SVP model. Although the classical barrier height of the reaction is negative, it is thought to affect the reactivity to a certain extent, possible due to the positive barrier height in the vibrationally adiabatic ground-state potential energy curve. The role of this kind of transition state deserves attention and further investigation.

Author Contributions: Conceptualization, H.S.; Investigation, Z.T.; Writing—original draft, Z.T. and H.S.; Writing—review & editing, Z.T., J.L., Y.W. and H.S.; Supervision, Y.W. and H.S.; Funding acquisition, H.S. and Y.W. All authors have read and agreed to the published version of the manuscript.

Funding: This work is supported by the National Natural Science Foundation of China under the Grant No. 21973109 to H.S. and No. 21963008 to Y.W.

Data Availability Statement: The data that support the findings of this study and the Fortran subroutine of the PES are available from the corresponding authors upon reasonable request.

Conflicts of Interest: The authors declare no conflict of interest.

References

- Zulfiqar, F.; Hancock, J.T. Hydrogen sulfide in horticulture: Emerging roles in the era of climate change. *Plant Physiol. Biochem.* **2020**, *155*, 667–675. [[CrossRef](#)] [[PubMed](#)]
- Cullis, C.F.; Hirschler, M.M. Atmospheric sulphur: Natural and man-made sources. *Atmos. Environ.* (1967) **1980**, *14*, 1263–1278. [[CrossRef](#)]
- Graedel, T.E. The homogeneous chemistry of atmospheric sulfur. *Rev. Geophys.* **1977**, *15*, 421–428. [[CrossRef](#)]
- Möller, D. Estimation of the global man-made sulphur emission. *Atmos. Environ.* (1967) **1984**, *18*, 19–27. [[CrossRef](#)]
- Hitchcock, D.R. Atmospheric Sulfates from Biological Sources. *J. Air Pollut. Control Assoc.* **1976**, *26*, 210–215. [[CrossRef](#)] [[PubMed](#)]

6. Beauchamp, R.O.; Bus, J.S.; Popp, J.A.; Boreiko, C.J.; Andjelkovich, D.A.; Leber, P. A Critical Review of the Literature on Hydrogen Sulfide Toxicity. *Crit. Rev. Toxicol.* **1984**, *13*, 25–97.
7. Jaeschke, W.; Claude, H.; Herrmann, J. Sources and sinks of atmospheric H₂S. *J. Geophys. Res. Oceans* **1980**, *85*, 5639–5644. [[CrossRef](#)]
8. Frenklach, M.; Lee, J.H.; White, J.N.; Gardiner, W.C. Oxidation of hydrogen sulfide. *Combust. Flame* **1981**, *41*, 1–16. [[CrossRef](#)]
9. Gargurevich, I.A. Hydrogen Sulfide Combustion: Relevant Issues under Claus Furnace Conditions. *Ind. Eng. Chem. Res.* **2005**, *44*, 7706–7729. [[CrossRef](#)]
10. Anderson, L.G. Atmospheric chemical kinetics data survey. *Rev. Geophys.* **1976**, *14*, 151–171. [[CrossRef](#)]
11. Westenberg, A.A.; deHaas, N. Rate of the reaction OH + H₂S → SH + H₂O over an extended temperature range. *J. Chem. Phys.* **1973**, *59*, 6685–6686. [[CrossRef](#)]
12. Perry, R.A.; Atkinson, R.; Pitts, J.N. Rate constants for the reactions OH + H₂S → H₂O + SH and OH + NH₃ → H₂O + NH₂ over the temperature range 297–427 °K. *J. Chem. Phys.* **1976**, *64*, 3237–3239. [[CrossRef](#)]
13. Wine, P.H.; Kreutter, N.M.; Gump, C.A.; Ravishankara, A.R. Kinetics of hydroxyl radical reactions with the atmospheric sulfur compounds hydrogen sulfide, methanethiol, ethanethiol, and dimethyl disulfide. *J. Phys. Chem.* **1981**, *85*, 2660–2665. [[CrossRef](#)]
14. Lin, C.L. Temperature dependence of the rate constant for the reaction OH + H₂S. *Int. J. Chem. Kinet.* **1982**, *14*, 593–598. [[CrossRef](#)]
15. Lin, Y.-L.; Wang, N.-S.; Lee, Y.-P. Temperature dependence of the rate constant for the reaction OH + H₂S in He, N₂, and O₂. *Int. J. Chem. Kinet.* **1985**, *17*, 1201–1214. [[CrossRef](#)]
16. Lafage, C.; Pauwels, J.-F.; Carrier, M.; Devolder, P. Rate constant for the reaction OH + H₂S in the range 243–463 K by discharge-flow laser-induced fluorescence. *J. Chem. Soc. Faraday Trans. 2* **1987**, *83*, 731–739. [[CrossRef](#)]
17. Wang, H.; Zhu, D.; Wang, W.; Mu, Y. The impact of HS radicals on the measured rate constant of H₂S with OH radicals. *Chin. Sci. Bull.* **2010**, *55*, 2951–2955. [[CrossRef](#)]
18. Wategaonkar, S.; Setser, D.W. Vibrational energy disposal in the reactions of F atoms with NH₃, ND₃, N₂H₄, and CH₃ND₂. *J. Chem. Phys.* **1987**, *86*, 4477–4487. [[CrossRef](#)]
19. Butkovskaya, N.I.; Setser, D.W. Chemical Dynamics of the OH and OD Radical Reactions with H₂S, CH₃SCH₃, and CH₃SH Studied by Infrared Chemiluminescence. *J. Phys. Chem. A* **1998**, *102*, 6395–6405. [[CrossRef](#)]
20. Butkovskaya, N.I.; Setser, D.W. Rate constants and vibrational distributions for water-forming reactions of OH and OD radicals with thioacetic acid, 1,2-ethanedithiol and tert-butanethiol. *Int. J. Chem. Kinet.* **2019**, *51*, 395–404. [[CrossRef](#)]
21. Butkovskaya, N.I.; Setser, D.W. Reactions of OH and OD radicals with simple thiols and sulfides studied by infrared chemiluminescence of isotopic water products: Reaction OH + CH₃SH revisited. *Int. J. Chem. Kinet.* **2021**, *53*, 702–715. [[CrossRef](#)]
22. Butkovskaya, N.I.; Setser, D.W. Reactions of OH and OD radicals with ethanethiol and diethylsulfide: Branching ratio and vibrational energy disposal for the product water molecules. *Chem. Phys.* **2022**, *555*, 111404. [[CrossRef](#)]
23. Wilson, C.; Hirst, D.M. Reaction of H₂S with OH and a study of the HSO and SOH isomers. High-level ab initio calculations. *J. Chem. Soc. Faraday Trans.* **1994**, *90*, 3051–3059. [[CrossRef](#)]
24. Mousavipour, S.H.; Namdar-Ghanbari, M.A.; Sadeghian, L. A Theoretical Study on the Kinetics of Hydrogen Abstraction Reactions of Methyl or Hydroxyl Radicals with Hydrogen Sulfide. *J. Phys. Chem. A* **2003**, *107*, 3752–3758. [[CrossRef](#)]
25. Ellingson, B.A.; Truhlar, D.G. Explanation of the Unusual Temperature Dependence of the Atmospherically Important OH + H₂S → H₂O + HS Reaction and Prediction of the Rate Constant at Combustion Temperatures. *J. Am. Chem. Soc.* **2007**, *129*, 12765–12771. [[CrossRef](#)]
26. Du, B.; Zhang, W. The effect of (H₂O)_n (n = 1–2) or H₂S on the hydrogen abstraction reaction of H₂S by OH radicals in the atmosphere. *Comput. Theor. Chem.* **2015**, *1069*, 77–85. [[CrossRef](#)]
27. Tang, M.; Chen, X.; Sun, Z.; Xie, Y.; Schaefer, H.F. The Hydrogen Abstraction Reaction H₂S + OH → H₂O + SH: Convergent Quantum Mechanical Predictions. *J. Phys. Chem. A* **2017**, *121*, 9136–9145. [[CrossRef](#)]
28. Ping, L.; Zhu, Y.; Li, A.; Song, H.; Li, Y.; Yang, M. Dynamics and kinetics of the reaction OH + H₂S → H₂O + SH on an accurate potential energy surface. *Phys. Chem. Chem. Phys.* **2018**, *20*, 26315–26324. [[CrossRef](#)]
29. Xiang, H.; Lu, Y.; Song, H.; Yang, M. Mode-Specific Quantum Dynamics Study of OH + H₂S → H₂O + SH Reaction. *Chin. J. Chem. Phys.* **2022**, *35*, 200–206. [[CrossRef](#)]
30. Michael, J.V.; Nava, D.F.; Brobst, W.D.; Borkowski, R.P.; Stief, L.J. Temperature dependence of the absolute rate constant for the reaction of hydroxyl radical with hydrogen sulfide. *J. Phys. Chem.* **1982**, *86*, 81–84. [[CrossRef](#)]
31. Leu, M.-T.; Smith, R.H. Rate constants for the gas-phase reaction between hydroxyl and hydrogen sulfide over the temperature range 228 to 518 K. *J. Phys. Chem.* **1982**, *86*, 73–81. [[CrossRef](#)]
32. Alday, B.; Johnson, R.; Li, J.; Guo, H. Hemibond complexes between H₂S and free radicals (F, Cl, Br, and OH). *Theor. Chem. Acc.* **2014**, *133*, 1540. [[CrossRef](#)]
33. Uchimaru, T.; Tsuzuki, S.; Sugie, M.; Tokuhashi, K.; Sekiya, A. A theoretical study on the strength of two-center three-electron bond in (CH₃)₂S–OH and H₂S–OH adducts. *Chem. Phys. Lett.* **2005**, *408*, 216–220. [[CrossRef](#)]
34. Shao, K.; Chen, J.; Zhao, Z.; Zhang, D.H. Communication: Fitting potential energy surfaces with fundamental invariant neural network. *J. Chem. Phys.* **2016**, *145*, 071101. [[CrossRef](#)] [[PubMed](#)]
35. Espinosa-García, J.; Bravo, J.L.; Rangel, C. New Analytical Potential Energy Surface for the F(²P) + CH₄ Hydrogen Abstraction Reaction: Kinetics and Dynamics. *J. Phys. Chem. A* **2007**, *111*, 2761–2771. [[CrossRef](#)] [[PubMed](#)]

36. Espinosa-García, J.; Bravo, J.L. State-to-State Dynamics Analysis of the F + CHD₃ Reaction: A Quasiclassical Trajectory Study. *J. Phys. Chem. A* **2008**, *112*, 6059–6065. [[CrossRef](#)]
37. Corchado, J.C.; Espinosa-García, J. Product Vibrational Distributions in Polyatomic Species Based on Quasiclassical Trajectory Calculations. *Phys. Chem. Chem. Phys.* **2009**, *11*, 10157–10164. [[CrossRef](#)]
38. Czako, G.; Bowman, J.M. Quasiclassical Trajectory Calculations of Correlated Product Distributions for the F+CHD₃(v₁ = 0, 1) Reactions Using an Ab Initio Potential Energy Surface. *J. Chem. Phys.* **2009**, *131*, 244302. [[CrossRef](#)]
39. Rauhut, G.; Knizia, G.; Werner, H.-J. Accurate calculation of vibrational frequencies using explicitly correlated coupled-cluster theory. *J. Chem. Phys.* **2009**, *130*, 054105. [[CrossRef](#)]
40. Shiozaki, T.; Werner, H.-J. Multireference explicitly correlated F12 theories. *Mol. Phys.* **2013**, *111*, 607–630. [[CrossRef](#)]
41. Werner, H.-J.; Knowles, P.J.; Knizia, G.; Manby, F.R.; Schuetz, M. Molpro: A general-purpose quantum chemistry program package. *Wiley Interdiscip. Rev. Comput. Mol. Sci.* **2012**, *2*, 242–253. [[CrossRef](#)]
42. Frisch, M.J.; Trucks, G.W.; Schlegel, H.B.; Scuseria, G.E.; Robb, M.A.; Cheeseman, J.R.; Scalmani, G.; Barone, V.; Petersson, G.A.; Nakatsuji, H.; et al. *Gaussian 09*, Revision B.01; Gaussian, Inc.: Wallingford, CT, UK, 2009.
43. Braams, B.J.; Bowman, J.M. Permutationally invariant potential energy surfaces in high dimensionality. *Int. Rev. Phys. Chem.* **2009**, *28*, 577–606. [[CrossRef](#)]
44. Xie, Z.; Bowman, J.M. Permutationally Invariant Polynomial Basis for Molecular Energy Surface Fitting via Monomial Symmetrization. *J. Chem. Theory Comput.* **2009**, *6*, 26–34. [[CrossRef](#)] [[PubMed](#)]
45. Hagan, M.T.; Menhaj, M.B. Training feedforward networks with the Marquardt algorithm. *IEEE Trans. Neural Netw.* **1994**, *5*, 989–993. [[CrossRef](#)] [[PubMed](#)]
46. Hase, W.L.; Duchovic, R.J.; Hu, X.; Komornicki, A.; Lim, K.F.; Lu, D.-H.; Peslherbe, G.H.; Swamy, K.N.; Vande Linde, S.R.; Varandas, A.; et al. VENUS96: A general chemical dynamics computer program. *Quantum Chem. Program Exch. Bull.* **1996**, *16*, 43.
47. Eaker, C.W.; Schatz, G.C.; De Leon, N.; Heller, E.J. Fourier Transform Methods for Calculating Action Variables and Semiclassical Eigenvalues for Coupled Oscillator Systems. *J. Chem. Phys.* **1984**, *81*, 5913–5919. [[CrossRef](#)]
48. Eaker, C.W.; Schatz, G.C. Semiclassical Vibrational Eigenvalues of Triatomic Molecules: Application of the FFT Method to SO₂, H₂O, H₃⁺, and CO₂. *J. Chem. Phys.* **1984**, *81*, 2394–2399. [[CrossRef](#)]
49. Skodje, R.T.; Borondo, F.; Reinhardt, W.P. The Semiclassical Quantization of Nonseparable Systems Using the Method of Adiabatic Switching. *J. Chem. Phys.* **1985**, *82*, 4611–4632. [[CrossRef](#)]
50. Espinosa-García, J.; Corchado, J.C. Quasi-Classical Trajectory Calculations of the Hydrogen Abstraction Reaction H + NH₃. *J. Phys. Chem. A* **2010**, *114*, 6194–6200. [[CrossRef](#)]
51. Espinosa-García, J. Quasi-Classical Trajectory Study of the Vibrational and Translational Effects on the O(³P) + CD₄ Reaction. *J. Phys. Chem. A* **2014**, *118*, 3572–3579. [[CrossRef](#)]
52. Ping, L.; Tian, L.; Song, H.; Yang, M. New Method To Extract Final-State Information of Polyatomic Reactions Based on Normal Mode Analysis. *J. Phys. Chem. A* **2018**, *122*, 6997–7005. [[CrossRef](#)]
53. Zhu, Y.; Ping, L.; Bai, M.; Liu, Y.; Song, H.; Li, J.; Yang, M. Tracking the Energy Flow in the Hydrogen Exchange Reaction OH + H₂O → H₂O + OH. *Phys. Chem. Chem. Phys.* **2018**, *20*, 12543–12556. [[CrossRef](#)]
54. Tian, L.; Zhu, Y.; Song, H.; Yang, M. Theoretical study of the F(²P) + NH₃ → HF + NH₂ reaction on an accurate potential energy surface: Dynamics and kinetics. *Phys. Chem. Chem. Phys.* **2019**, *21*, 11385–11394. [[CrossRef](#)] [[PubMed](#)]
55. Czako, G. Gaussian Binning of the Vibrational Distributions for the Cl + CH₄(v_{4/2} = 0, 1) → H + CH₃Cl(n₁n₂n₃n₄n₅n₆) Reactions. *J. Phys. Chem. A* **2012**, *116*, 7467–7473. [[CrossRef](#)] [[PubMed](#)]
56. Jiang, B.; Guo, H. Relative efficacy of vibrational vs. translational excitation in promoting atom-diatom reactivity: Rigorous examination of Polanyi's rules and proposition of sudden vector projection (SVP) model. *J. Chem. Phys.* **2013**, *138*, 234104. [[CrossRef](#)]
57. Guo, H.; Jiang, B. The Sudden Vector Projection Model for Reactivity: Mode Specificity and Bond Selectivity Made Simple. *Acc. Chem. Res.* **2014**, *47*, 3679–3685. [[CrossRef](#)] [[PubMed](#)]
58. Jiang, B.; Li, J.; Guo, H. Effects of reactant rotational excitation on reactivity: Perspectives from the sudden limit. *J. Chem. Phys.* **2014**, *140*, 034112. [[CrossRef](#)]
59. Jiang, B.; Yang, M.; Xie, D.; Guo, H. Quantum dynamics of polyatomic dissociative chemisorption on transition metal surfaces: Mode specificity and bond selectivity. *Chem. Soc. Rev.* **2016**, *45*, 3621–3640. [[CrossRef](#)]

Disclaimer/Publisher's Note: The statements, opinions and data contained in all publications are solely those of the individual author(s) and contributor(s) and not of MDPI and/or the editor(s). MDPI and/or the editor(s) disclaim responsibility for any injury to people or property resulting from any ideas, methods, instructions or products referred to in the content.